separations

MDPI

Article

Inorganic–Organic Hybrid Polymer for Fine-Rich Coal Slime Water Treatment: Performance and Interfacial Adsorption Mechanism on Kaolinite Aluminol Surface

Jing Chang [1,2], Hang Zhao [1], Shizhen Liang [1], Xihao Feng [1], Jia Xue [3] and Wei Zhao [1,*]

[1] College of Chemistry and Chemical Engineering, Xi'an University of Science and Technology, Xi'an 710054, China; jchang@xust.edu.cn (J.C.); h18045979656@163.com (H.Z.); 22415030123@stu.xust.edu.cn (S.L.); 18591868600@163.com (X.F.)
[2] Key Laboratory of Coal Processing & Efficient Utilization, Ministry of Education, Xuzhou 221008, China
[3] Yifeng Jiuyu Lithium Co., Ltd., Yichun 336304, China; xuejia@greenjiuling.com
* Correspondence: zhaowei3859520@163.com; Tel.: +89-134-8495-4405

Abstract

High-ash coal slime water, characterized by its stable colloidal suspension of fine kaolinite particles, poses a significant challenge in the coal preparation industry because it is hard to achieve efficient solid–liquid separation. While traditional coagulants and flocculants often suffer from limited bridging capabilities and distinct pH sensitivity, novel molecular architectures offer potential solutions. In this study, a star-shaped inorganic–organic hybrid flocculant (Al-PAM) was synthesized via in situ polymerization. Its flocculation performance and interfacial adsorption mechanism on the specifically targeted aluminol basal plane of kaolinite were systematically investigated and compared with Polyaluminum Chloride (PAC), Non-ionic Polyacrylamide (NPAM), and their combination (PAC + NPAM). Settling tests revealed that Al-PAM exhibited superior performance at a significantly lower dosage (10 mg·L^{-1}) compared to the PAC + NPAM binary reagent system. It achieved a rapid initial settling velocity and reduced the supernatant turbidity to 48.45 NTU, while maintaining a near-neutral pH favorable for water recycling. Furthermore, Quartz Crystal Microbalance with Dissipation (QCM-D) monitoring confirmed that Al-PAM forms a thick, viscoelastic, and irreversible adsorption layer on the Al_2O_3 substrate. The dissipation shifts (ΔD) revealed that the star-shaped architecture promotes distinct bridging and electrostatic adsorption, overcoming the limitation of linear polymers. This work elucidates the specific contribution of the alumina-surface interaction with flocculants and proposes an efficient strategy for treating refractory coal slime water.

Keywords: fine-rich coal slurry; dewatering; star-shaped flocculant; kaolinite aluminol surface; adsorption mechanism

Check for updates

Academic Editors: Ruxia Chen and Zeyu Feng

Received: 24 February 2026
Revised: 17 March 2026
Accepted: 17 March 2026
Published: 19 March 2026

Copyright: © 2026 by the authors. Licensee MDPI, Basel, Switzerland. This article is an open access article distributed under the terms and conditions of the Creative Commons Attribution (CC BY) license.

1. Introduction

In 2024, amid post-pandemic recovery and energy market volatility, the world witnessed record highs in coal production, consumption, trade, and coal-fired power generation. Nowadays, coal still serves as a pivotal component of the global energy structure, accounting for approximately 33% of supply [1–3]. As the world's largest coal consumer, China is forecast to account for nearly 50% of the global boost in electricity demand through 2030 [3]. This rising demand, fueled by the accelerating electrification of industry and the expansion of high-tech sectors like AI, underscores coal's continued indispensability for its affordability

and 24/7 dispatchability. In China, the extensive use of wet coal preparation process inevitably generates massive quantities of coal slime water, a complex colloidal suspension containing fine minerals [4–7]. With deeper mining and increased mechanization, raw coal carries more fines and clay minerals, which readily disperse in water and are hard to separate [8]. However, efficiently clarifying and recycling this process water is critical for environmental protection, water resource conservation, and economic sustainability of coal preparation plants [9].

Recycling water from coal slime water is challenging due to the high content of fine-grained solid particles (<0.045 mm), which typically carry negative charges. These charges cause electrical repulsion surpassing the attractive van der Waals forces among fine particles, hindering sedimentation without effective aggregation [10–13]. The solid components in coal slime water are primarily inorganic minerals [14]. Studies on the mineral composition of coal from representative mining areas in China have revealed that clay minerals (<2 μm) are the dominant phase, with kaolinite, illite, and montmorillonite being the most common species [15–17]. Quantitative analyses by Zhang et al. of coal samples from the Linhuan, Datun, Xingtai, and Zaozhuang mining areas further demonstrate that clay minerals account for over 70% of the inorganic matter in most cases, with kaolinite alone comprising between 46.76% and 75.68% of the clay fraction [18]. These clay minerals easily disintegrate into microfine particles in aqueous environments, making them a major component of coal slime water and significantly complicating its treatment.

Kaolinite, a dominant and representative clay mineral, is a phyllosilicate with complex surface characteristics. Its particles feature two chemically distinct basal planes: the siloxane tetrahedral surface (Si-surface) and the aluminum oxy-hydroxyl octahedral surface (Al-surface) [19]. This surface heterogeneity significantly complicates interactions among particles and between chemical reagents and mineral surfaces [20].

In coal slime water treatment, coagulation and flocculation are the most widely used methods to destabilize this colloidal suspension, aggregating fine particles into larger flocs to accelerate solid–liquid separation. The most commonly used coagulant is polyaluminum chloride (PAC), which functions primarily through charge neutralization and electrical double layer compression [21,22]. However, the flocs formed by PAC are typically small and loose, limiting their effectiveness in enhancing settling rates [23]. It is also easy to overdose PAC due to fluctuations in the concentration of high-valence cations present in the process water, thus causing charge reversal of the negatively charged coal slime particles to become positively charged and re-stabilize the system. To promote particle bridging, organic polymer flocculants such as polyacrylamide (PAM) are often employed alongside coagulants [24]. Nevertheless, linear polymers like PAM surface challenges in bridging efficiency when dealing with high-concentration fine tailings, as their chains may not extend sufficiently to capture distant particles. Moreover, the flocculation of kaolinite by PAM is highly sensitive to the chemical conditions of aqueous environment, particularly pH and the presence and concentration of hydrolyzable metal ions. These factors significantly alter the interfacial chemistry of kaolinite, which in turn governs PAM adsorption behavior and flocculation performance [25]. Excessive residual PAM in the recycled water increases its viscosity, which can impair downstream pressure filtration and upper stream flotation. This has led to the development of architecturally modified flocculants (see Table 1), such as Hyperbranched Polyester, Aluminum-Polyacrylamide (Al-PAM), Aluminum Hydroxide-poly(N-isopropylacrylamide-co-N,N-dimethylaminoethyl methacrylate) [$Al(OH)_3$-p(NIPAM-co-DMAPMA)], etc. [9,26–39]. Among these, the inorganic-organic hybrid Al-PAM has emerged as a particularly promising flocculant due to its distinct star-shape structure, with PAM chains extending radially from a central $Al(OH)_3$ core [26]. This unique configuration equipped the flocculant with dual functionality: the

cationic core facilitates electrostatic charge neutralization, whereas the extended PAM chains mediate efficient interparticle bridging [27].

Table 1. Quantitative Comparison of Flocculant Performance for Coal Slime Water Treatment.

Flocculant Type		Flocculant Name	Flocculant Dosage	Coal Slime Water Properties/ Concentration (C *)	Settling Velocity ($cm \cdot min^{-1}$)	Sediment Properties	Supernatant Clarity	Ref. *
TR *	Inorganic Coagulant	Polyaluminum Chloride (PAC)	15 $kg \cdot t^{-1}$	C = 40 $g \cdot L^{-1}$	Approx. 6	Not specified	Low (Superior to PAS and PFS)	[30]
	Anionic Organic Flocculant	Anionic Polyacrylamide (APAM, MW 6 million)	100 $g \cdot t^{-1}$	D * < 0.074 mm, C = 20 $g \cdot L^{-1}$	79	Large floc particle size; Fractal dimension 1.635	Transmittance 78%	[31]
	Cationic Organic Flocculant	Cationic Polyacrylamide (CPAM)	50 $g \cdot t^{-1}$	d_{50} = 26.61 µm, Ash 49.58%, contains kaolinite, quartz, calcite	72.08	Sediment height 5.1 cm	Transmittance 89.1%	[32]
	Cationic Organic Flocculant	Cationic Polyacrylamide (CPAM, MW 6 million)	250 $g \cdot t^{-1}$	d < 0.074 mm, C = 20 $g \cdot L^{-1}$	18.38	Small floc particle size; Fractal dimension 1.602	Transmittance 56%	[33]
	Non-ionic Organic Flocculant	Non-ionic Polyacrylamide (NPAM)	90 $g \cdot t^{-1}$	d_{50} = 26.61 µm, Ash 49.58%, contains kaolinite, quartz, calcite	Low	Sediment height 6.5 cm	Transmittance 68%	[32]
	Non-ionic Organic Flocculant	Non-ionic Polyacrylamide (NPAM, MW 6 million)	250 $g \cdot t^{-1}$	d < 0.074 mm, C = 20 $g \cdot L^{-1}$	Low	Medium floc particle size; Fractal dimension 1.618	Transmittance 67%	[33]
	Organic/Inorganic Composite	Polyaluminum Chloride (PAC) + Cationic Polyacrylamide (CPAM)	PAC: 50 $g \cdot t^{-1}$ CPAM: 50 $g \cdot t^{-1}$	d_{50} = 26.61 µm	75.38	Sediment height 4.5 cm	Transmittance 96.2%	[32]
NF *	Cationic Organic Flocculant	Chitosan-acrylamide-dimethyldiallylammonium chloride graft copolymer (CS-g-ADM)	6 $mg \cdot L^{-1}$	C = 20 $g \cdot L^{-1}$, pH 8.74	63	Sediment height 2.2 cm; Filter cake moisture 21.95%	Transmittance 93%	[34]
	Cationic Organic Flocculant	P(DMDAAC-AM) (PDA) copolymer	Optimal dosage ≤ 200 $g \cdot t^{-1}$	Fine coal slime water	Highly improved	Filter cake moisture increased; Larger flocs, higher fractal dimension (1.86)	Specific values not provided	[9]
	Novel Flocculant (TG) alone	Novel Flocculant TG	70 $g \cdot t^{-1}$	C = 40 $g \cdot L^{-1}$, 74.88% d < 0.045 mm	33.33	Sediment height 2.9 cm	111 NTU	[35]
	Novel Flocculant (TG) + CPAM	Novel Flocculant TG + Cationic Polyacrylamide (CPAM)	TG:60 $g \cdot t^{-1}$ CPAM:20 $g \cdot t^{-1}$	C = 40 $g \cdot L^{-1}$, 74.88% d < 0.045 mm	50	Sediment height 2.3 cm	39 NTU	[35]
	Organic/ Inorganic Composite	Novel Purifying Agent (BK819A, containing N-(2-aminopropyl)acrylamide fragment)	5 $mg \cdot L^{-1}$	C = 20 $g \cdot L^{-1}$	16.8 $mL \cdot min^{-1}$	-	91 NTU	[36]
	Inorganic Composite Flocculant	Poly-silicic aluminum ferric sulfate (PSAFS)	0.2 $g \cdot L^{-1}$ (relative to slime water)	Initial turbidity 133.8 NTU	Large flocs, easy to settle	Not specified	Turbidity removal rate > 95%	[37]
	Composite Agent	Sodium polyacrylate-polyacrylamide copolymer (flocculant) + Diallyl dimethyl ammonium chloride (coagulant)	Optimal ratio 5:1	C = 21.7 $g \cdot L^{-1}$	Highly improved	Not specified	Circulating water C = 0.5 $g \cdot L^{-1}$	[38]
	Organic-inorganic Composite Flocculant	Aluminum Hydroxide–Polyacrylamide (Al-PAM)	6 $mg \cdot L^{-1}$	62.49% d < 0.045 mm, C = 30 $g \cdot L^{-1}$	84	2.3 cm	45.77 NTU	[39]

* Footnote: TR stands for Traditional Reagents (including coagulants and flocculants); NF stands for Novel Flocculants; Ref. stands for References; d stands for particle size; C stands for concentration.

Understanding the adsorption mechanism of these reagents at the solid–liquid interface is fundamental to optimizing their performance. Although extensive studies have utilized techniques such as adsorption tests, atomic force microscopy, and Fourier transform infrared spectroscopy to investigate polymer adsorption on clay minerals, these investigations either primarily focused on the total adsorption amount on whole clay particles without distinguishing between different crystallographic faces, or on the adsorption morphology [40,41]. More quantitative insights into adsorption mechanisms on clay mineral surfaces have been achieved using Quartz Crystal Microbalance with Dissipation (QCM-D). However, most QCM-D studies concentrated on silica or the Si-surface of clay mineral, primarily because this surface can be conveniently represented by a silica sensor or a mica-coated QCM-D sensor, while the Al-surface has been largely overlooked due to the lack of such an accessible model surface [28,39,42,43]. The omission is significant because the Al-surface, one of kaolinite's two basal planes, is amphoteric. Its aluminol groups can protonate or deprotonate depending on pH, substantially impacting reagent adsorption. Neglecting the Al-surface thus results in an incomplete understanding of the flocculation mechanism for anisotropic clay minerals.

In this study, a novel star-shaped Al-PAM was synthesized via in situ polymerization. Unlike previous studies that focused primarily on the siloxane surface or bulk interactions, this work specifically targets the previously overlooked aluminol surface of kaolinite to elucidate its role in Al-PAM adsorption and flocculation performance. Its flocculation performance was systematically evaluated in the treatment of refractory coal slime water, with PAC, NPAM, and the PAC + NPAM composite as reference systems. To address the research gap in understanding the adsorption mechanisms of reagents on the Al-surface of anisotropic kaolinite, the adsorption kinetics and viscoelastic properties of the adsorbed layer were investigated using QCM-D. This work aims to elucidate the specific contributions of the star-shaped structure and its interfacial interactions with the Al-surface of kaolinite to the coagulation-flocculation process. Together with our previous findings on the Si-surface [39], this study provides a comprehensive understanding of the adsorption mechanism, thereby offering a theoretical basis for designing high-efficiency flocculants tailored for anisotropic clay mineral systems.

2. Materials and Methods

2.1. Materials

To ensure consistency between the flocculant settling performance and adsorption mechanism investigations in coal slime water treatment, we used the same coal slime sample as in our previous study [39]. Obtained from the Zhengtong Coal Preparation Plant (Xi'an, China), this sample contains kaolinite as its predominant mineral constituent (see Figure S1 in the Supporting Information). The main chemicals used to synthesize the desired Al-PAM flocculants included: acrylamide (AR, 99.0%), ammonium carbonate (AR), ammonium persulfate (AR, ≥98%), and sodium bisulfite (99.99%), all purchased from Shanghai Aladdin Biochemical Technology Co., Ltd., Shanghai, China; anhydrous aluminum chloride (99%) and nonionic polyacrylamide (NPAM-500, molecular weight ~5 million) was obtained from Shanghai Macklin Biochemical Technology Co., Ltd., Shanghai, China; polyaluminum chloride (PAC) was purchased from Tianjin Damao Chemical Reagent Factory, Tianjin, China. All organic solvents were of analytical grade and supplied by Tianjin Fuyu Fine Chemical Co., Ltd. (Tianjin, China).

2.2. Synthesis of Al-PAM

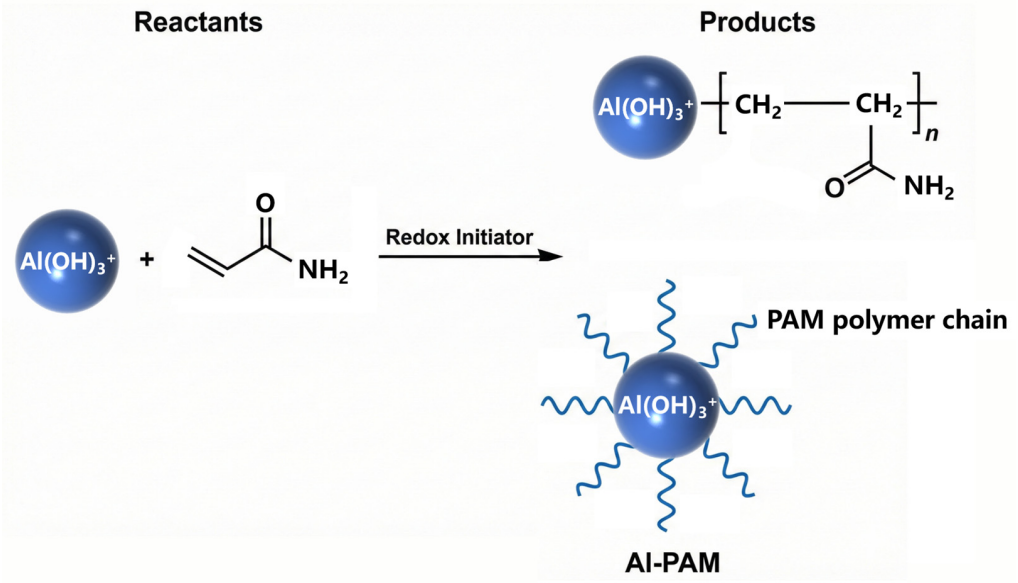
In this study, a novel star-shaped Al-PAM was synthesized via in situ polymerization. The use of aluminum hydroxide as a core component aligns with emerging strategies that repurpose aluminum-based materials for high-performance applications, such as in catalysis for biomass conversion [44].

Preparation of Aluminum Hydroxide Colloid: At room temperature, 36 g of 0.1 M ammonium carbonate solution was added dropwise with a micro-peristaltic pump at a rate of 0.5 g·min^{-1} into 25 g of 0.1 M aluminum chloride solution under continuous stirring at 500 rpm. After the addition, stirring was continued at 300 rpm for 1 h, yielding an $Al(OH)_3$ colloid according to Equation (1).

$$2AlCl_3 + 3(NH_4)_2CO_3 + 3H_2O \longrightarrow 2Al(OH)_3\ (Colloid) + 6NH_4Cl + 3CO_2\uparrow \quad (1)$$

In Situ Polymerization: The synthesis procedure for Al-PAM, depicted in Scheme 1, began with the addition of 4.5 g of acrylamide and 25.5 mL of freshly prepared $Al(OH)_3$ colloid to a 100 mL three-necked flask. This mixture was then stirred at 250 rpm for 30 min in a 40 °C water bath under a nitrogen atmosphere and light-shielded condition. Following this, 2 mL of a redox initiator solution (consisting of 0.125 g·L^{-1} ammonium persulfate and 0.0625 g·L^{-1} sodium bisulfite) was introduced dropwise at 0.13 g·min^{-1}. After 10 min,

both the stirring and the nitrogen flow were discontinued, and the reactor was sealed. The polymerization was then carried out statically at 40 °C for 6 h, resulting in a transparent polymer gel.



Scheme 1. Schematic illustration of Al-PAM synthesis and structure.

Purification and Drying: Unreacted monomers and initiators were removed from the synthesized polymer gel through a dissolution-reprecipitation purification process. The gel was first dissolved in ultrapure water under mechanical stirring to obtain a 5 wt.% homogeneous solution. To induce polymer precipitation, the solution was added dropwise to a coagulation bath containing 60% ethanol in water. The gathered precipitate was subjected to multiple washing cycles using the ethanol/water solution, followed by an acetone rinse to remove any lingering reactants. The purified material was subsequently dried in a vacuum oven at 55 °C until a constant weight was achieved (approximately 8 h), after which it was ground and stored in a polypropylene (PP) centrifuge tube for subsequent use.

2.3. Molecular Weight Determination of Al-PAM

Using an Ubbelohde viscometer (0.6–0.7 mm, Sinopharm Chemical Reagent Co., Ltd., Shanghai, China), the viscosity-average molecular weight (M_η) of the synthesized Al-PAM was determined via intrinsic viscosity measurements.

A 0.04 wt.% polymer solution was obtained by dissolving 0.02 g of Al-PAM in 50 mL of ultrapure water. The completely dissolved sample was introduced into a 100 mL volumetric flask and diluted with 50 mL of 2 mol·L^{-1} NaCl solution. The flask was then filled to the mark with ultrapure water and thoroughly mixed.

The efflux time of the pure solvent (t_0) was first measured using 1 mol·L^{-1} NaCl solution. Both the solvent and sample solutions were allowed to equilibrate in a water bath at 30 ± 0.1 °C for 15 min prior to measurement. The efflux time of the sample solution (t) was measured under the same conditions. Three replicate measurements were conducted and the results were averaged for subsequent calculation, with the error between replicates not exceeding 0.2 s.

The intrinsic viscosity [η] was calculated using the following equation:

$$[\eta] = \frac{\sqrt{2(\eta_{sp} - \ln \eta_r)}}{\rho} \quad (2)$$

where $\eta_r = \frac{t_1}{t_0}$ is the relative viscosity, $\eta_{sp} = \eta_r - 1$ is the specific viscosity, and ρ is the mass concentration of the polymer solution ($g \cdot mL^{-1}$).

The viscosity-average molecular weight was then obtained from the Mark-Houwink equation:

$$[\eta] = K \cdot M_\eta^\alpha \quad (3)$$

where the constants $K = 6.3 \times 10^{-3}$ and $\alpha = 0.8$ were adopted for polyacrylamide under the given conditions [27,45].

2.4. Fourier Transform Infrared Spectroscopy (FTIR) Measurement

Fourier transform infrared spectroscopy (FTIR) was performed using a Nicolet iN10&iZ10 spectrometer (Thermo Fisher Scientific, Waltham, MA, USA). The KBr pellet method was adopted, where Al-PAM pure PAM and pure $Al(OH)_3$ were thoroughly mixed with KBr at a mass ratio of 1:100 and pressed into transparent pellets for measurement, respectively. FTIR spectra were recorded in the range of 4000–400 cm^{-1} with a spectral resolution of 4 cm^{-1}.

2.5. Settling Tests

To replicate the plant's typical coal slurry, which has an approximate ash content of 42.5%, crushed raw coal and gangue were blended at a 2:1 mass ratio to prepare a simulated coal slime sample with an ash content of 40.43%. The particle size distribution of the sample was determined to be: 7.14% > 0.125 mm, 18.47% between 0.074 and 0.125 mm, 11.90% between 0.045 and 0.074 mm, and 62.49% < 0.045 mm. The high proportion of ultrafine particles confirms its suitability as a representative model for studying difficult-to-settle, heavily muddied coal slime water at a solid concentration of 30 $g \cdot L^{-1}$. This concentration is typical for the sampled plant and falls within the range commonly reported in the literature [9,30–39]. Even at this concentration, the untreated suspension remains extremely stable due to its high fines content, necessitating chemical treatment. Higher concentrations were not investigated because they would prevent the PAC-only control group from yielding measurable settling data.

Reagent solutions were prepared one day prior to use following typical plant concentrations: PAC at 0.5 wt.%, and NPAM-500 and Al-PAM at 0.1 wt.%. For each, 500 ± 0.5 g of ultrapure water was stirred at 800 rpm in a 1000 mL beaker; after a sufficiently large vortex was formed, the reagent was added and stirred at 400 rpm until fully dissolved. The solution was then made up to 1000 mL in a volumetric flask with ultrapure water.

The settling performance of the reagents was evaluated using the settling tests. A 30 $g \cdot L^{-1}$ coal slime suspension was first prepared by agitation with a magnetic stirrer (MS-H280-Pro, Dalong Xingchuang, Beijing, China) at 700 rpm for 5 min to ensure homogeneity. The well-mixed suspension was then transferred to a 500 mL graduated settling cylinder and inverted 5 times to achieve a uniform initial state. Following the addition of a predetermined dosage of coagulant or flocculant, the cylinder was again inverted 5 times to ensure thorough mixing. The settling process was then monitored by recording the descent of the mud line over time. Using the recorded data, a settling curve was generated by plotting the normalized mud line height (h/H) against settling time, where h represents the momentary mud line height and H denotes the initial suspension height. The initial settling rate (ISR) was derived from the slope of the linear portion of this curve at the start of settling.

To evaluate solid–liquid separation efficiency and colloidal stability, supernatant samples were collected after 10 min of settling. Immediately after recording the sediment thickness, supernatant samples were carefully extracted from a fixed depth of 10 cm below the liquid surface. A 30 mL portion of this supernatant was used for turbidity measurement

with a WZS-188 turbidimeter (Shanghai Leici, Shanghai, China). Concurrently, another sample was taken for zeta potential determination, which was performed at 25 °C using a ZEN3690 analyzer (Malvern Panalytical, Malvern, UK). All measurements were conducted in triplicate on the supernatant as collected, without any further dilution or pretreatment.

2.6. Quartz Crystal Microbalance with Dissipation (QCM-D) Measurement

QCM-D measurements were conducted using a Q-Sense Explorer instrument to investigate the adsorption behavior of the reagents on model mineral surfaces. To simulate the Al-surface of kaolinite present in coal slime, AT-cut quartz crystal sensors (fundamental frequency 5 MHz) coated with α-Al_2O_3—deposited via a vapor deposition process optimized to favor exposure of the (0001) plane—were employed. Prior to each test, the sensors were sequentially cleaned with 2 wt.% sodium dodecyl sulfate (SDS) solution for 30 min, rinsed thoroughly with ultrapure water, dried with nitrogen gas, and finally subjected to UV-ozone treatment for 20 min to ensure a clean, hydrophilic surface.

At a constant temperature of 20.0 ± 0.2 °C, ultrapure water was first introduced at a flow rate of 0.15 mL·min^{-1} until stable frequency (f) and dissipation (D) signals were achieved, serving as the baseline. The flow was then switched to the reagent solution (PAC: 5000 ppm; NPAM, PAC-NPAM, Al-PAM: 100 ppm), and the real-time changes in f and D were monitored (primarily using the third overtone data). After adsorption reached equilibrium or a predetermined time, the flow was switched back to ultrapure water for rinsing to observe desorption behavior. A negative shift in frequency (Δf) indicates mass adsorption onto the sensor surface; a positive shift in dissipation (ΔD) suggests a softer, more hydrated adsorbed layer. The instrument's accompanying Dfind software (QSense Dfind version 1.2.7, Biolin Scientific, Sweden) was employed, utilizing the Voigt viscoelastic model to fit multi-harmonic data (3rd, 5th, and 7th overtones). The Voigt model was selected because our polymer solution exhibits viscoelastic behavior rather than purely liquid-like response, as established by Voinova et al. [46], the Voigt model is applicable for polymers that conserve their shape and do not flow, whereas the Maxwell model is typically used for liquid-like systems. This model assumes a homogeneous, uniformly thick layer with rigid anchoring to the sensor surface and no slip at the interface—assumptions widely accepted in QCM-D studies of polymer adsorption and successfully applied to characterize thick, highly hydrated polymer layers [47] and the growth of viscoelastic films [48]. This fitting enabled enabling the calculation of adsorbed mass and the shear modulus of the adsorbed layer for quantitative comparison of the layer structures formed by different reagents. We adopted the Voigt model because our polymer solution is viscous and not purely liquid-like. Published work has also demonstrated that this model remains valid for adsorbed layers that are thick, viscoelastic, soft and hydrated, or densely packed—characteristics consistent with the layers observed in our study. To ensure reporting consistency, all Δf and ΔD data reported were obtained from measurements performed at the third overtone due to its consistently good signal-to-noise ratio. The displayed QCM-D data are representative of consistent trends observed across replicate measurements.

2.7. Microscopic Imaging of Floc Structure

A 1 L sample of coal slime water with a concentration of 30 g·L^{-1} was placed in a beaker and thoroughly dispersed to ensure uniformity. Following the addition of the reagent, the mixture was stirred at 700 rpm for 1 min, followed by a 10 min quiescent settling period. Flocs sedimented at the bottom of the beaker were carefully collected using a large-bore sampling tube and transferred to a Petri dish. Images of the flocs were captured using a Leica DM4P microscope system (Leica Microsystems, Wetzlar, Germany).

3. Results and Discussion

3.1. Characterization of Synthesized Al-PAM

The inorganic-organic hybrid flocculant Al-PAM synthesized following the method detailed in Section 2.2 was analyzed using Fourier transform infrared spectrometer (FTIR). The FTIR spectrum illustrated in Figure 1 provides evidence for the successful synthesis of the $Al(OH)_3$-PAM.

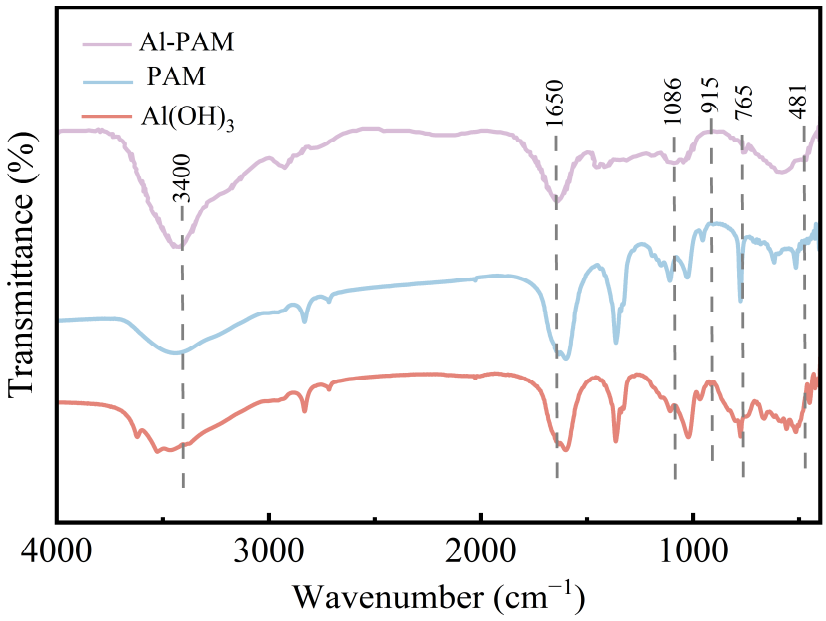


Figure 1. FTIR Spectrum of Al-PAM hybrid, pure PAM, and pure $Al(OH)_3$.

The spectrum simultaneously displays characteristic absorption peaks attributable to both the inorganic $Al(OH)_3$ component and the organic PAM component. In the low wavenumber region, absorption peaks at 765 cm^{-1} and 481 cm^{-1} are assignable to Al-O related vibrations (such as Al-O-Al bending or Al-O stretching) of the inorganic $Al(OH)_3$ component, confirming the presence of the inorganic aluminum-oxygen framework. Characteristic features of PAM are evidenced by: a broad band centered around 3400 cm^{-1} corresponding to overlapping N-H and O-H stretching vibrations, a strong band at ~1650 cm^{-1} attributed to the amide I band (C=O stretching vibration).

Further analysis indicates that the interaction between the two components is not a simple physical mixture but involves chemical interaction. This interaction is primarily manifested in the shift of the Al-O-H bending vibration. In pure $Al(OH)_3$, the in-plane bending vibration of Al-O-H typically appears at approximately 915 cm^{-1}. However, in the spectrum of the hybrid, this absorption band exhibits a significant blue shift to 1086 cm^{-1}. This shift is attributed to the formation of strong hydrogen bonding interactions between the hydroxyl groups on the $Al(OH)_3$ framework and the amide groups of the PAM chains during the in situ polymerization process [49]. This conclusion is corroborated by the observed broadening of the amide group absorption bands in the spectrum. These spectral features collectively indicate the successful formation of a chemically interacting hybrid structure, consistent with the FTIR spectral characteristics reported in the literature for Al-PAM hybrid flocculants based on ionic bonding [50].

The zeta potential of the synthesized Al-PAM was determined to be +0.60 mV in a 1000 ppm aqueous solution, confirming its cationic nature, which enables electrostatic attraction with negatively charged mineral surfaces. Using the molecular weight determi-

nation method described in Section 2.3, the viscosity-average molecular weight of Al-PAM was determined to be 4.42 × 10^6 Da.

3.2. Settling Performance

The synthesized Al-PAM was systematically evaluated not only for its coagulation-flocculation-sedimentation performance but also in direct comparison with the reference coagulant PAC, flocculant NPAM, and the PAC + NPAM combination. For a rigorous comparison, each reagent was dosed at its optimal concentration established in our preliminary studies [51]: PAC at 60 mg·L^{-1}, NPAM at 20 mg·L^{-1}, Al-PAM at a remarkably lower dosage of 10 mg·L^{-1}, and the binary regimen comprising 60 mg·L^{-1} PAC followed by 10 mg·L^{-1} NPAM. Key performance indicators, including supernatant turbidity, pH, ISR, and sediment layer thickness are presented and discussed below.

3.2.1. Supernatant Turbidity and pH

Supernatant turbidity is a critical indicator for determining whether recycled water meets environmental discharge or reuse standards. As shown in Figure 2a, the individual application of either PAC or NPAM failed to effectively clarify the high-ash and fine-rich coal slime water, resulting in high supernatant turbidity avlues of approximately 178.76 NTU and 171.43 NTU, respectively. The binary PAC + NPAM reagent system significantly improved the clarification performance, lowering the turbidity to 62.47 NTU. Most notably, Al-PAM alone exhibited outstanding solid–liquid separation efficiency. At an exceptionally low dosage of 10 mg·L^{-1}, Al-PAM achieved a supernatant turbidity of 48.45 NTU, surpassing the performance of the binary reagent system while consuming only 1/7th of its total chemical dosage (10 mg·L^{-1} vs. 70 mg·L^{-1}). This suggests that Al-PAM successfully integrates both charge neutralization and bridging functions, efficiently capturing fine particles that escape removal by linear polymers and conventional coagulants.

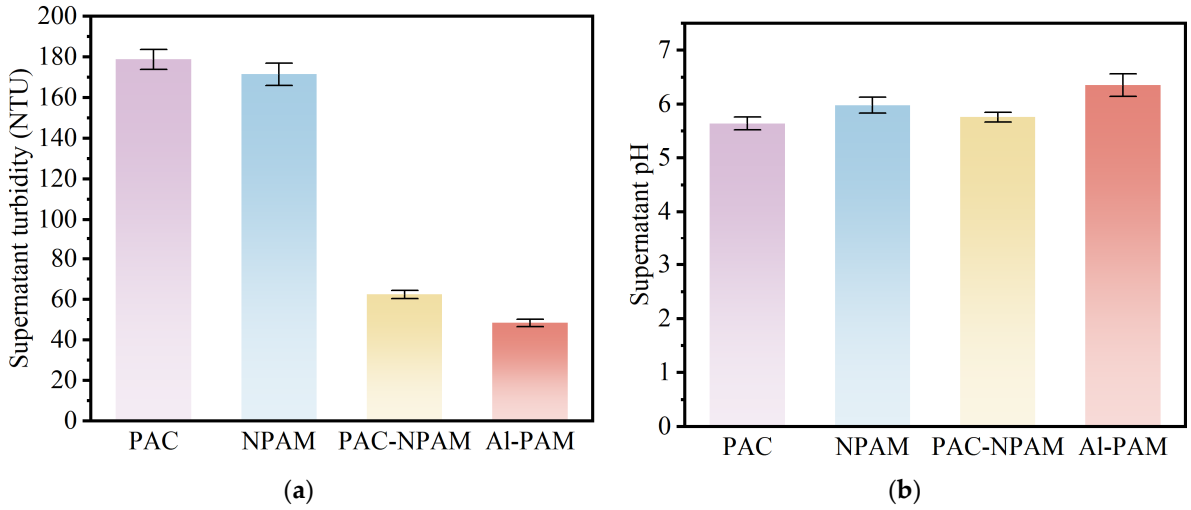


Figure 2. Comparison of (**a**) supernatant turbidity and (**b**) supernatant pH of coal slime water treated with Al-PAM and reference reagents at optimal dosages (PAC: 60 mg·L^{-1}; NPAM: 20 mg·L^{-1}; PAC + NPAM: 60 mg·L^{-1} PAC + 10 mg·L^{-1} NPAM; Al-PAM: 10 mg·L^{-1}).

Beyond its superior clarification ability, Al-PAM exhibited a distinct advantage in maintaining supernatant pH close to a neutral level. In coal preparation plants, the pH of the circulating water is not actively adjusted by the addition of acids or bases during the slime water treatment process. This makes the intrinsic pH of the treated water a critical operational factor, because corrosion prevention in the circulating water systems accounts for a large portion of operational cost [52,53]. Therefore, supernatant pH is a key consideration

for equipment maintenance, as deviations from neutrality can highly enhance the corrosion rates and increase expenditures. As shown in Figure 2b, treatments using high-dosage PAC (both individually and binary reagent applications) resulted in more acid supernatant with pHs of 5.64 and 5.76, respectively, levels that may pose corrosion risks. In contrast, Al-PAM-treated water maintained a near-neutral pH of approximately 6.35, demonstrating its advantage in preserving water neutrality and mitigating potential equipment corrosion.

This distinct pH behavior can be attributed to the differences in the chemical structures and the reaction mechanisms of PAC and Al-PAM. When PAC (polyaluminum chloride, $[Al_2(OH)_nCl_{6-n}]_m$) is introduced into water, it dissociates to release Al^{3+} ions, which then undergo stepwise hydrolysis, releasing H^+ ions as follows:

$$Al^{3+} + H_2O \rightarrow Al(OH)^{2+} + H^+ \quad (4)$$

$$Al(OH)^{2+} + H_2O \rightarrow Al(OH)_2^+ + H^+ \quad (5)$$

$$Al(OH)_2^+ + H_2O \rightarrow Al(OH)_3 + H^+ \quad (6)$$

At the high dosage of PAC (60 mg·L^{-1}), the substantial quantity of Al^{3+} ions continuously generates H^+ through these hydrolysis reactions, progressively acidifying the water to pH 5.64–5.76.

In contrast, the synthesized Al-PAM comprises $Al(OH)_3$ cores ionically bonded to multiple PAM arms. When Al-PAM is applied to coal slime water, its $Al(OH)_3$ cores function as solid buffers. The abundant surface hydroxyl groups (−OH) can reversibly consume or release H^+ through protonation/deprotonation reactions:

$$Al - OH + H^+ \rightleftharpoons Al - OH_2^+ \quad (7)$$

This protonation reaction not only generates positively charged sites (Al-OH_2^+) responsible for the measured zeta potential of +0.6 mV and the electrostatic attraction to overall negatively charged particles (−26.8 mV), but also actively consumes free H^+ from solution, preventing pH decline. Thus, Al-PAM maintains the supernatant pH at approximately 6.35 due to the buffering capacity of its $Al(OH)_3$ cores, a mechanism that avoids the acidification inherent to PAC hydrolysis.

3.2.2. Settling Velocity and Sediment Layer Thickness

The ISR and the final mud line height (i.e., the sediment layer thickness) were investigated and the results are given in Figure 3. Because the coal slime water treated only by PAC failed to form a distinct mud line during the observation period due to insufficient coagulation ability, which resulted in high supernatant turbidity (178.76 NTU) that obscured the sedimentation interface, its corresponding ISR and sediment layer thickness were not recorded.

As shown in Figure 3a, the ISR of the coal slime water treated by NPAM alone was 107.43 cm·min^{-1}. However, the extremely high supernatant turbidity suggests that this rapid settling was primarily driven by the sedimentation of coarse agglomerates, leaving ultrafine particles still suspended in the supernatant. With the addition of PAC prior to NPAM, the ISR further increased to 130.90 cm·min^{-1}, indicating enhanced particle aggregation first through charge neutralization followed by bridging flocculation. Al-PAM alone achieved an ISR of 75.61 cm·min^{-1} at a substantially lower dosage (10 mg·L^{-1}). Although this settling velocity is lower than that of the PAC + NPAM system, it is fully adequate for coal slime water treatment [32], while offering superior supernatant clarity and requiring substantially less chemical consumption.

The sediment layer thickness provided in Figure 3b reflects the compactness and potential dewaterability of the resulting sludge. Among all the four reagent treatments, the PAC + NPAM system produced the thickest sediment layer (2.7 cm), suggesting the

formation of porous, "fluffy" flocs that entrap substantial interstitial water, which may hinder subsequent mechanical dewatering. NPAM alone produced a sediment layer of 2.3 cm. However, the high supernatant turbidity (~171 NTU, Figure 2a) suggests that while NPAM formed settlable aggregates via bridging flocculation, it failed to capture the ultrafine particles due to the absence of charge neutralization ability. Consequently, the 2.3 cm sediment probably consists of loosely bound, porous flocs that retain considerable interstitial water. Notably, Al-PAM yielded the most compact sediment layer (2.2 cm) despite its lower ISR and significantly reduced dosage. This indicates that the unique star-shaped architecture of Al-PAM, with its inorganic $Al(OH)_3$ core and radiating PAM chains, promotes the formation of denser, more compressible flocs. Such compact sediment facilitates water exclusion and enhances underflow concentration, offering distinct advantages for downstream dewatering operations.

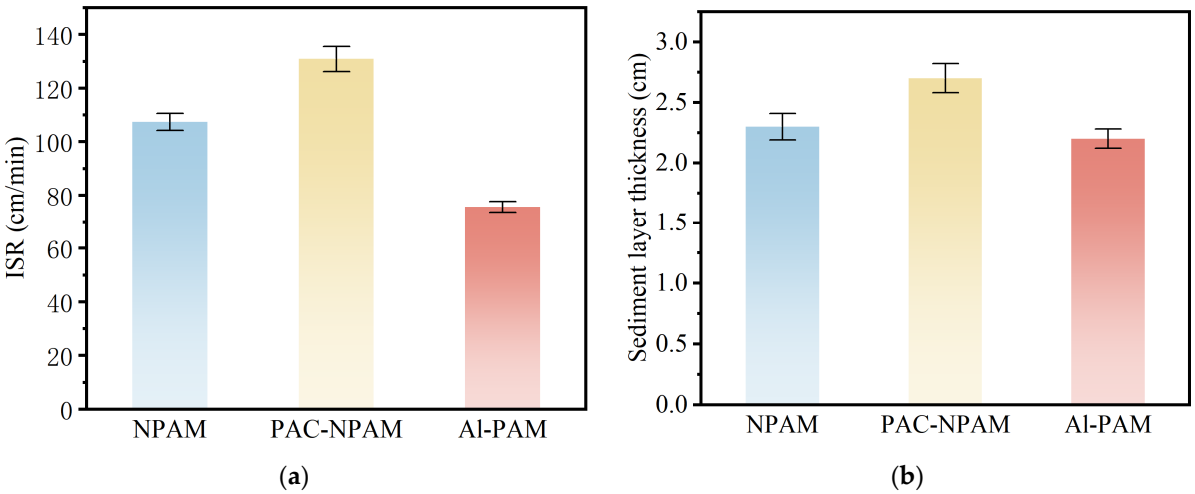


Figure 3. Comparison of (**a**) initial settling rate and (**b**) sediment layer thickness of coal slime water treated with Al-PAM and reference reagents at optimal dosages (NPAM: 20 mg·L^{-1}; PAC + NPAM: 60 mg·L^{-1} PAC + 10 mg·L^{-1} NPAM; Al-PAM: 10 mg·L^{-1}).

3.3. Floc Structure

To directly visualize the structural characteristics underlying the observed differences in sedimentation and consolidation behavior, flocs formed by each treatment (PAC, NPAM, PAC + NPAM, and Al-PAM) were examined and representative images are given in Figure 4.

3.3.1. PAC Flocs

As shown in Figure 4a, coal slime particle flocs formed with the addition of PAC were very small and compact. These flocs exhibited a large length-to-width ratio, suggesting that the high-valence cations from PAC primarily neutralized the negative surface charge of the clay minerals, which inherently possess a layered structure with a high aspect ratio. This charge neutralization likely promoted basal-to-basal association between clay particles. However, PAC alone was insufficient to aggregate the majority of the clay minerals, resulting in flocs that remained extremely small in size. According to Stokes' law, such small flocs settle slowly, which explains the unclear mud line, the unmeasurable ISR and the high supernatant turbidity observed in PAC settling test.

3.3.2. NPAM Flocs

Figure 4b reveals that NPAM generated flocs substantially larger than those of PAC, but with abundant remaining fine particles. Notably, numerous fine particles remained suspended in the background, indicating incomplete aggregation. This morphological

observation aligns well with the macroscopic settling behavior of NPAM: the enlarged floc size accounts for the increased ISR; the persistent presence of fine particles explains the still-high supernatant turbidity (~171 NTU); and the moderately compact sediment layer (2.3 cm) reflects the porous yet settlable nature of the flocs.

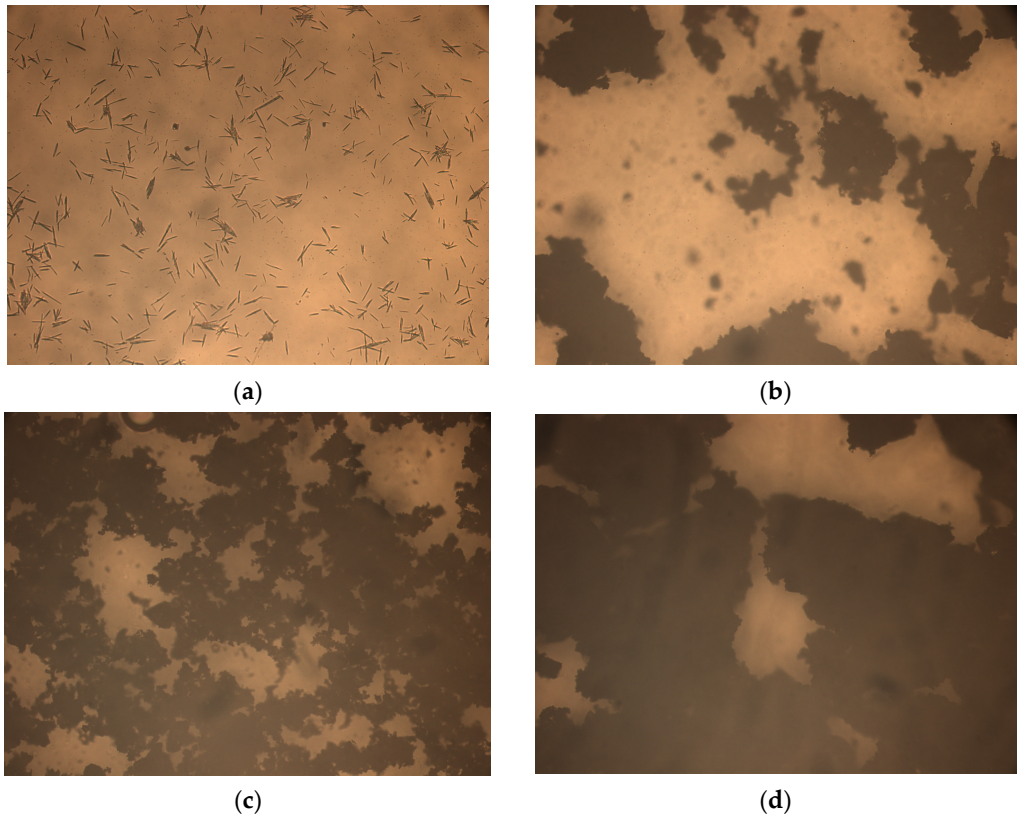


Figure 4. Microscopic imaging of coal slime flocs (200×) formed by different treatments: (**a**) PAC; (**b**) NPAM; (**c**) PAC + NPAM; (**d**) Al-PAM.

3.3.3. PAC + NPAM Flocs

As seen in Figure 4c, the PAC + NPAM binary system produced continuous but structurally loose and "fluffy" flocs with visible inter-particle voids, as predicted from the sedimentation and consolidation behavior. Although the long-chain NPAM effectively bridged the PAC-neutralized particles to achieve excellent supernatant clarity, the resulting network was not dense enough so that water was retained within the sediment. This explains the macroscopic performance of the PAC + NPAM system: the highest ISR, intermediate supernatant turbidity, and the thickest sediment layer, indicating a loosely packed sediment structure that may pose challenges for downstream mechanical dewatering.

3.3.4. Al-PAM Flocs

The flocs formed by the Al-PAM hybrid polymer (Figure 4d) exhibited a remarkably different microstructure. These flocs appeared large, compact and dense, with well-defined boundaries and minimal internal voids. This densification directly results from the unique star-shaped architecture of Al-PAM. The rigid inorganic $Al(OH)_3$ core acts as a robust anchor point, while the radial PAM arms enable multi-point bridging without forming overly extended, water-entrapping loops characteristic like linear polymers. As a result, these dense flocs possess a higher density, leading to a rapid ISR and the highest supernatant clarity. Moreover, the compact floc minimizes water retention during aggregation, offering a structural basis for Al-PAM's superior consolidation performance: achieving the thinnest sediment layer (2.2 cm).

3.4. Adsorption Mechanisms

The settling tests and floc structure analysis revealed that both the PAC + NPAM binary system and Al-PAM achieved rapid settling and high supernatant clarity, but Al-PAM formed much more compact flocs, resulting in a thinner sediment layer. The contrast between the "fluffy" nature of PAC + NPAM flocs and the "dense" structure of Al-PAM flocs points to fundamental differences in how these polymers interact with the mineral surfaces. To elucidate these differences, this study specifically focuses on the Al-surface of kaolinite, a critical yet often overlooked basal plane of clay minerals in coal slime water treatment. Building on our previous investigation of adsorption mechanisms on the Si-surface, this work aims to provide a comprehensive understanding of the interfacial interactions between coagulants/flocculants and clay mineral surfaces.

3.4.1. Adsorption of PAC

As illustrated in Figure 5a, the injection of PAC induced a rapid frequency drop (Δf) to −7 HZ and stabilized at approximately −9 Hz, accompanied by a dissipation (ΔD) increase to about 3.0×10^{-6}. Upon rinsing with ultrapure water, substantial desorption occurs, yet a residual frequency shift and mass uptake (~650 ng/cm^2, Figure 5c) remain, indicating that a fraction of PAC is irreversibly anchored to the alumina surface. The non-overlapping adsorption–desorption trajectories in the ΔD-Δf plot (Figure 5b) further confirm that desorption does not simply reverse the adsorption path, and that part of the adsorption layer is firmly retained.

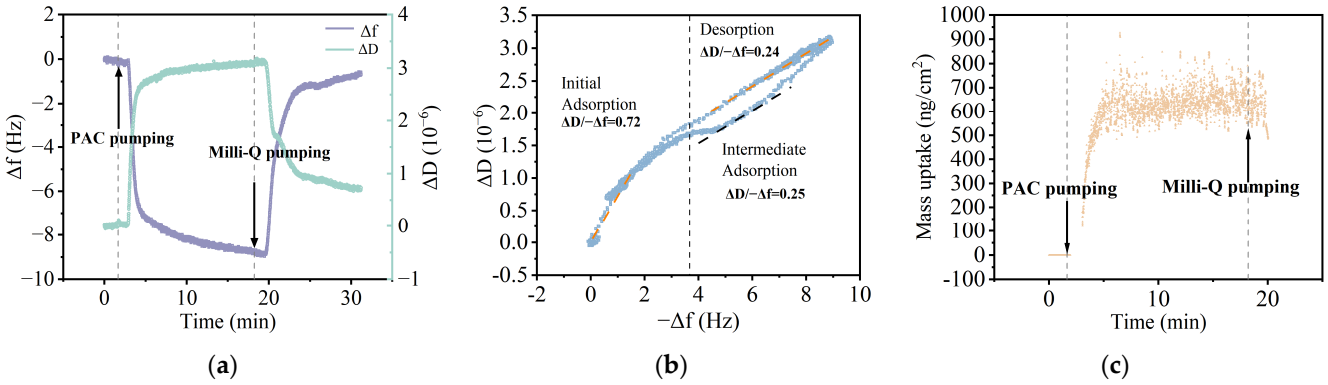


Figure 5. Adsorption kinetics of PAC on an alumina sensor. (**a**) Time-resolved frequency/dissipation shifts; (**b**) ΔD-Δf plots; (**c**) Mass uptake over time.

Notably, this partially irreversible attachment occurred despite the likelihood of electrostatic repulsion between PAC and the alumina surface. PAC is known to acidify aqueous solutions as discussed above, and given that the point of zero charge (PZC) of alumina lies between 6 and 8 [20], the surface is expected to be positively charged under the slightly acidic conditions created by PAC itself. Therefore, the observed adsorption cannot be primarily driven by electrostatic attraction, it more likely arises from specific non-electrostatic interactions, such as hydrogen bonding and ligand exchange between PAC hydroxyl groups and surface aluminol sites.

Mechanistically, PAC adsorption on Al_2O_3 exhibited a two-stage conformational evolution. The initial adsorption phase was characterized by a relatively high $\Delta D/-\Delta f$ slope of approximately 0.72×10^{-6}/Hz, indicating the formation of a soft, hydrated layer with a moderately extended structure. However, as adsorption progresses, the slope decreases markedly to about 0.25×10^{-6}/Hz, suggesting a gradual structural rearrangement toward a more compact and rigid configuration. Despite this initial flexibility, PAC ultimately forms a relatively compact adsorption layer that lacks long, extended polymer chains

essential for effective bridging flocculation. Consequently, PAC's flocculation mechanism remains confined to short-range charge neutralization and patch flocculation, failing to capture ultrafine particles. This microscopic picture directly explains the macroscopic observations: PAC alone generates only minute, needle-like flocs that settle slowly, leaving high supernatant turbidity (178.76 NTU). The inability to form long-range bridging structures confines PAC's action to short-range charge screening and local charge neutralization.

3.4.2. Adsorption of NPAM

As shown in Figure 6a, the introduction of NPAM onto the alumina surface triggered a profound and rapid frequency drop (Δf) to approximately −68 Hz, which corresponds to a massive mass uptake of nearly 2600 ng/cm^2 (Figure 6c). Unlike the highly reversible adsorption of PAC, rinsing with Milli-Q water caused negligible desorption, with the Δf curve showing only a slight recovery. This demonstrates that NPAM binds strongly and irreversibly to the alumina surface, a process likely driven by hydrogen bonding between the amide groups of the polymer and the aluminol sites on the Al-surface, supplemented by van der Waals interactions.

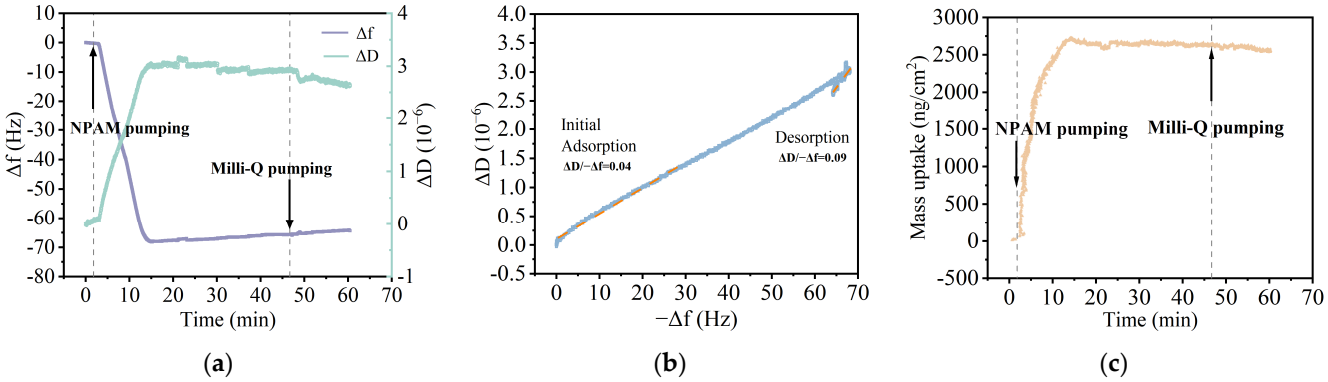


Figure 6. Adsorption kinetics of NPAM on an alumina sensor. (**a**) Time-resolved frequency/dissipation shifts; (**b**) ΔD-Δf plots; (**c**) Mass uptake over time.

Despite its strong and irreversible adsorption on the alumina surface (Figure 6a), NPAM exhibits a critical functional limitation revealed by its conformation. The ΔD-Δf plot (Figure 6b) displays an exceptionally linear trajectory with an extremely low slope ($\Delta D/\Delta f \approx 0.04 \times 10^{-6}$/Hz), indicating that the adsorbed NPAM chains are in a rigid, dehydrated, and densely packed conformation. Rather than forming extended loops and tails essential for bridging flocculation, the polymer spreads flatly on the surface, accumulating through multilayer stacking with minimal chain extension into the solution. This lack of spatial extension fundamentally restricts the effective bridging range. Consequently, although this dense coating enables rapid agglomeration of coarse particles, it fails to capture ultrafine clay particles. This leads to a high ISR but unacceptably high supernatant turbidity (171.43 NTU). At last, the layer-by-layer accumulation of rigid NPAM chains produces flocs that retain substantial interstitial water due to their poorly organized internal structure, yielding a moderately compact sediment layer (2.3 cm) as observed in Section 3.2.

3.4.3. Adsorption of PAC + NPAM

As depicted in Figure 7a, the sequential addition of PAC and NPAM reveals the interfacial synergy of the binary coagulation-flocculation system. Initially, the addition of PAC causes a small frequency drop (Δf), serving as an electrostatic "primer" on the alumina surface. Upon the subsequent addition of NPAM, Δf further decreases rapidly to approximately −95 Hz, accompanied by a dramatic increase in the dissipation factor (ΔD)

to nearly 7.1 × 10^{-6}. Unlike the highly reversible adsorption of adding PAC alone, the washing step with Milli-Q water induces negligible desorption, which is comparable to the irreversible adsorption behavior of NPAM, demonstrating that this composite adsorption layer is robustly anchored to the alumina surface.

The conformational evolution depicted in the ΔD-Δf plot (Figure 7b) significantly differs from the single-reagent systems. The trajectory exhibits a pronounced upward trend with an initial high slope of 0.31 × 10^{-6}/Hz, followed by a lower slope of 0.04 × 10^{-6}/Hz, indicating a fundamental structural transformation during the adsorption process. Facilitated by the PAC adsorption base layer, the subsequently adsorbed NPAM chains no longer adopt the rigid conformation observed for NPAM alone, they extend outward into the bulk solution, forming a hydrated, soft, and viscoelastic layer. This extended spatial architecture confers exceptional bridging capabilities, successfully sweeping ultrafine particles to achieve outstanding supernatant clarity (62.47 NTU). However, the highly hydrated and soft nature of this composite layer is structurally consistent with its operational drawbacks: the extended network traps significant interstitial water, directly leading to the formation of the observed "fluffy" flocs and the elevated sediment layer thickness (2.7 cm).

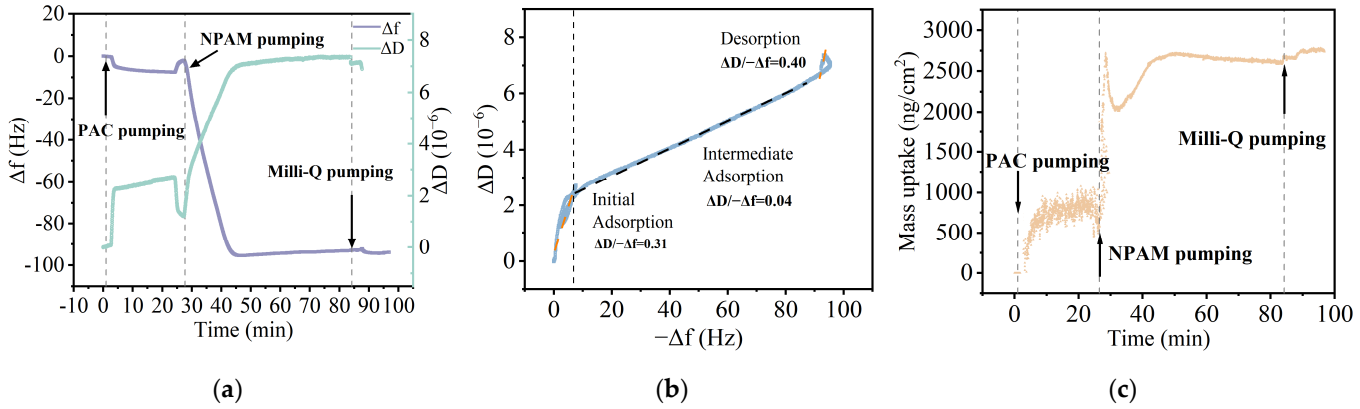


Figure 7. Adsorption kinetics of PAC-NPAM on an alumina sensor. (**a**) Time-resolved frequency/dissipation shifts; (**b**) ΔD-Δf plots; (**c**) Mass uptake over time.

3.4.4. Adsorption of Al-PAM

Al-PAM exhibits a distinctive adsorption profile on the alumina surface, as presented in Figure 8a. The frequency (Δf) gradually decreases and stabilizes at approximately −6.5 Hz, corresponding to a moderate mass uptake of roughly 550 ng/cm^2 (Figure 8c). Upon rinsing with Milli-Q water, both Δf and ΔD curves remain very stable with negligible desorption. This confirms that the cationic $Al(OH)_3$ core of Al-PAM serves as an effective anchor, forming strong, irreversible bonds with the alumina surface. This robust anchoring is likely driven primarily by hydrogen bonding between the hydroxyl groups of the $Al(OH)_3$ core and the aluminol sites on the surface. This is consistent with the findings of Yao et al., who reported that hydrogen incorporation in polymers significantly enhances interfacial binding with aluminum oxide surfaces, facilitating subsequent reactions [54]. Additionally, under the near-neutral pH conditions induced by Al-PAM, the alumina surface may carry a slight negative charge (as its PZC lies between 6 and 8), which could further enhance adsorption through electrostatic attraction.

While the strong anchoring of Al-PAM is notable, its conformational characteristics provide even deeper insight into its superior flocculation performance. The ΔD-Δf plot (Figure 8b) exhibits a steep linear trajectory with an initial high ΔD/−Δf ratio of approximately 0.76 × 10^{-6}/Hz, followed by an intermediate slope of 0.52 × 10^{-6}/Hz. Despite the relatively small frequency shift, the dissipation reaches nearly 4.4 × 10^{-6}, indicating that

the adsorbed layer is flexible, hydrated, and highly active for bridging. This high ΔD/−Δf ratio demonstrates that, while the inorganic core firmly anchors to the alumina surface, the radial PAM arms extend outward into the bulk solution, forming a viscoelastic and spatially extended three-dimensional structure optimized for bridging flocculation.

Crucially, unlike the PAC + NPAM binary system that achieved bridging capability at the cost of excessive mass uptake (>2500 ng/cm^2) and water entrapment, Al-PAM constructs an efficient bridging network using only one-seventh of the dosage. This elegant star-shaped architecture enables effective capture of ultrafine particles while simultaneously allowing interstitial water to be expelled during aggregate formation. Such microscopic structural balance determines the macroscopic performance of Al-PAM observed in Sections 3.2 and 3.3: the formation of dense, rapidly settling flocs, the thinnest sediment layer (2.2 cm), an excellent dewaterability and a superior supernatant clarity (48.45 NTU), all achieved at an ultralow chemical dosage.

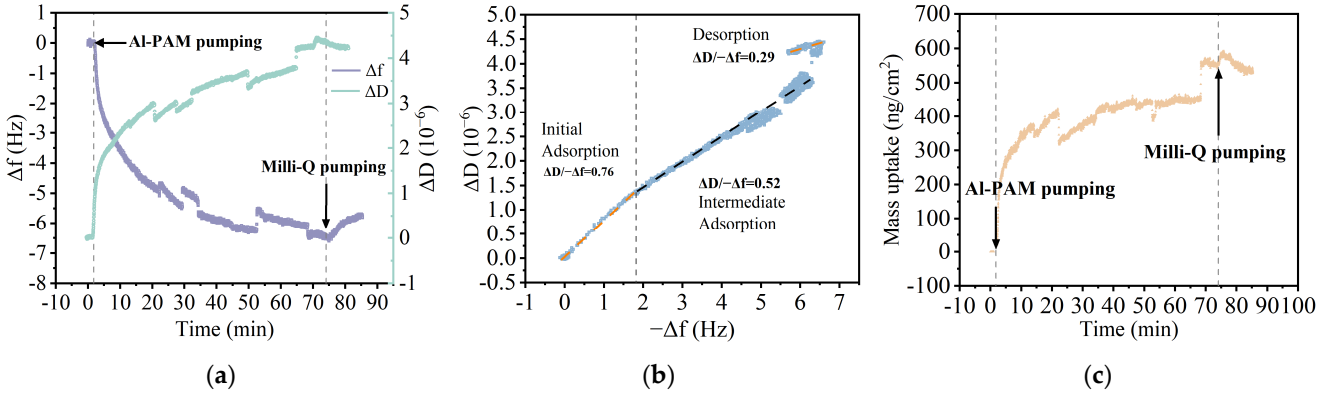


Figure 8. Adsorption kinetics of Al-PAM on an alumina sensor. (**a**) Time-resolved frequency/dissipation shifts; (**b**) ΔD-Δf plots; (**c**) Mass uptake over time.

4. Conclusions

This study successfully synthesized a star-shaped inorganic-organic hybrid polymer (Al-PAM) and systematically evaluated its performance in treating high-ash, fine-rich coal slime water, with particular focus on elucidating its adsorption mechanism on the aluminol basal plane of kaolinite to establish a clear structure-activity relationship between polymer adsorption configuration and macroscopic dewatering performance. Compared to the benchmark agents (PAC, NPAM) and the binary PAC + NPAM system, Al-PAM exhibited superior coagulation-flocculation-sedimentation efficiency, achieving a supernatant turbidity of 48.45 NTU at an ultralow dosage of 10 mg·L^{-1} while forming the most compact sediment layer (2.2 cm). In contrast, although the PAC + NPAM combination achieved rapid settling, it produced highly hydrated, loose flocs resulting in a thicker sediment layer (2.7 cm) and a higher supernatant turbidity (62.47 NTU) with a total chemical dosage of 70 mg·L^{-1}. QCM-D analysis revealed that the star-shaped architecture of Al-PAM exhibits a rigid-core/flexible-arm adsorption configuration. This configuration provides strong surface anchoring while enabling effective particle bridging without excessive water entrapment, thereby explaining its superior coal slime water treatment performance. Additionally, Al-PAM maintained near-neutral supernatant pH (~6.35), offering benefits for water recycling and equipment corrosion mitigation. This work provides new theoretical insights into the flocculant adsorption mechanisms on anisotropic clay minerals and proposes a robust strategy for designing hybrid flocculants tailored for complex solid–liquid separation processes. However, this work only explored the adsorption mechanisms of Al-PAM in ultrapure water; it is of great interest to systematically investigate the impact

of water chemistry of real industrial water (such as the kinds of cations present and their ionic strength) in future studies.

Furthermore, for researchers aiming to apply Al-PAM-treated fine-rich suspensions in pipeline transportation, investigating the shear-induced breakup behavior or transport properties of the flocs would be a valuable extension of this work.

Supplementary Materials: The following supporting information can be downloaded at: https://www.mdpi.com/article/10.3390/separations13030099/s1, Figure S1: XRD diffractogram for mineral composition analysis of the coal slime sample. (This figure is cited in Section 2.1 of the main text).; Table S1: Mineral phases identified by XRD and their semi-quantitative (S-Q) results.

Author Contributions: Conceptualization, J.C.; methodology, W.Z.; validation, J.X. and X.F.; formal analysis, H.Z.; investigation, H.Z.; writing—original draft preparation, S.L.; writing—review and editing, J.C.; visualization, S.L.; supervision, W.Z.; funding acquisition, J.C. All authors have read and agreed to the published version of the manuscript.

Funding: This research was funded by Open Funding of the Key Laboratory of Coal Processing and Efficient Utilization, Ministry of Education, grant number JSK202404; Xi'an Association for Science and Technology Young Elite Scientists Sponsorship Program, grant number 959202413002; and 2024 Annual Xi'an University of Science and Technology Excellent Youth Science Foundation Project: Study on the Structure of Hydration layers on Clay Mineral Surfaces and the Regulatory Mechanisms of Aggregation-Dispersion Behavior of Fine Mineral Particles.

Data Availability Statement: The original contributions presented in this study are included in the article/Supplementary Materials. Further inquiries can be directed to the corresponding author.

Conflicts of Interest: Author Jia Xue is employed by the company Yifeng Jiuyu Lithium Co., Ltd. The remaining authors declare that the research was conducted in the absence of any commercial or financial relationships that could be construed as a potential conflict of interest.

Abbreviations

The following abbreviations are used in this manuscript:

Al-PAM	Aluminum hydroxide-polyacrylamide
PAC	Polyaluminum chloride
PAM	Polyacrylamide
QCM-D	Quartz crystal microbalance with dissipation monitoring
SDS	Sodium dodecyl sulfate
$Al(OH)_3$-p(NIPAM-co-DMAPMA)	Aluminum Hydroxide-poly(N-isopropylacrylamide-co-N,N-dimethylaminoethyl methacrylate)

References

1. Saletnik, A.; Saletnik, B.; Puchalski, C. Coal as the world's dominant energy source and its role in the energy transformation and regulations of European Green Deal. *J. Environ. Manag.* **2025**, *392*, 126815. [CrossRef]
2. IEA. Coal Analysis and Forecast to 2027. Available online: https://www.repower.world/news/iea-coal-analysis-and-forecast-to-2027-a-summary (accessed on 15 January 2026).
3. Jones, A. Coal's Share in Global Generation Mix to Slip. Available online: https://www.argusmedia.com/en/news-and-insights/latest-market-news/2786338-coal-s-share-in-global-generation-mix-to-slip-iea (accessed on 10 January 2026).
4. Sabah, E.; Erkan, Z.E. Interaction mechanism of flocculants with coal waste slurry. *Fuel* **2006**, *85*, 350–359. [CrossRef]
5. Li, L.; Zhang, X.; Luo, J.; Hu, B. Theoretical Analysis of the Movement Law of Top Coal and Overburden in a Fully Mechanized Top-Coal Caving Face with a Large Mining Height. *Processes* **2022**, *10*, 2596. [CrossRef]
6. Chen, X.; Peng, Y. Managing clay minerals in froth flotation—A critical review. *Miner. Process. Extr. Metall. Rev.* **2018**, *39*, 289–307. [CrossRef]
7. Fan, Y.; Ruan, C.; Chang, M.; Dong, X.; Ma, X.; Ye, G. Effect of settling vortex of coal slime flocs with different sizes on the settlement of microfine particles. *Powder Technol.* **2025**, *452*, 120422. [CrossRef]

8. Pan, F.; Ding, S.; Zou, H. Research status of genesis analysis and treatment technology of difficult-to-settle slime water. *Coal Process. Compr. Util.* **2023**, *3*, 9–14. [CrossRef]
9. Wang, L.; Min, F.; Sun, K.; Chen, J.; Cheng, Y.; Song, C. Exploration of interaction between different types of flocculants and coal particles based on experiments and simulations. *Surf. Interfaces* **2025**, *59*, 105903. [CrossRef]
10. Fan, Y.; Chang, T.; Zhang, J.; Xu, H.; Cui, J.; Tian, H.; Yin, Y. Research on influence of CPAM ionic degree on settling characteristics of high muddied coal slime water. *Coal Sci. Technol.* **2023**, *51*, 251–260. [CrossRef]
11. Nguyen, C.V.; Nguyen, A.V.; Doi, A.; Dinh, E.; Nguyen, T.V.; Ejtemaei, M.; Osborne, D. Advanced solid-liquid separation for dewatering fine coal tailings by combining chemical reagents and solid bowl centrifugation. *Sep. Purif. Technol.* **2021**, *259*, 118172. [CrossRef]
12. Eskibalci, M.F.; Ozkan, M.F. Comparison of conventional coagulation and electrocoagulation methods for dewatering of coal preparation plant. *Miner. Eng.* **2018**, *122*, 106–112. [CrossRef]
13. Zhang, W.; Dong, Z.; Han, X. Experimental study on flocculation and settlement of slime water in Guantun Coal Mine Preparation Plant. *Coal Process. Compr. Util.* **2023**, *02*, 51–56. [CrossRef]
14. Han, Y.H. Quantum Chemistry Study on the Surface Properties and Dispersion Mechanism of Kaolinite and Montmorillonite. Ph.D. Thesis, China University of Mining and Technology (Beijing), Beijing, China, 2017.
15. Zhang, M.Q.; Liu, J.T.; Liu, H.H.; Wang, Y.T. Effects of water hardness on the dispersion of fine coal and montmorillonite. *J. China Univ. Min. Technol.* **2009**, *38*, 114–118.
16. He, M.; Yang, X.; Sun, X. *Study on Clay Mineral Characteristics of Soft Rock in Chinese Coal Mines*; China Coal Industry Publishing House: Beijing, China, 2006.
17. Chen, Q.; Li, P.; Wei, X.; Chen, C.; Dang, W.; Nie, H.; Zhang, J. Mineralogy and geochemistry of shale from Shanxi Formation, Southern North China Basin: Implication for organic matter accumulation. *Unconv. Resour.* **2025**, *6*, 100151. [CrossRef]
18. Zhang, Z.J.; Liu, J.T. Settling Characteristics Analysis of Coal Slime Water Based on Original Hardness. *J. China Coal Soc.* **2014**, *39*, 757–763. [CrossRef]
19. Tombácz, E.; Szekeres, M. Surface charge heterogeneity of kaolinite in aqueous suspension in comparison with montmorillonite. *Appl. Clay Sci.* **2006**, *34*, 105–124. [CrossRef]
20. Chang, J.; Shao, H.; Liu, B.; Manica, R.; Li, Z.; Liu, Q.; Xu, Z. Control of nanostructures through pH-dependent self-assembly of nanoplatelets. *J. Colloid Interface Sci.* **2021**, *582*, 439–445. [CrossRef]
21. Fan, Y.P.; Dong, X.S.; Li, H. Study on Sedimentation and Dehydration of Oxidized Coal with Hydrogen Peroxide. *Coal Technol.* **2015**, *34*, 308–310. [CrossRef]
22. Li, G.C.; Yan, X.H.; Li, M.M. EDLVO Analysis of Flocculation and Sedimentation of Slime Water under PAC. *J. Heilongjiang Univ. Sci. Technol.* **2020**, *30*, 45–49.
23. Li, Y.; Chen, C.; Xia, W.; Sun, Y.; Qiu, H. Flocculation of sodium alginate combined with $AlCl_3$/PAC on fine calcite: An in-situ experimental and calculation study. *Appl. Surf. Sci.* **2025**, *682*, 161692. [CrossRef]
24. Xu, S.; Shi, J.; Deng, J.; Sun, H.; Wu, J.; Ye, Z. Flocculation and dewatering of the Kaolin slurry treated by single- and dual-polymer flocculants. *Chemosphere* **2023**, *328*, 138445. [CrossRef]
25. Mpofu, P.; Addai-Mensah, J.; Ralston, J. Influence of hydrolyzable metal ions on the interfacial chemistry, particle interactions, and dewatering behavior of kaolinite dispersions. *J. Colloid Interface Sci.* **2003**, *261*, 349–359. [CrossRef] [PubMed]
26. Sun, W.; Long, J.; Xu, Z.; Masliyah, J.H. Study of $Al(OH)_3$−Polyacrylamide-Induced Pelleting Flocculation by Single Molecule Force Spectroscopy. *Langmuir* **2008**, *24*, 14015–14021. [CrossRef]
27. Alagha, L.; Wang, S.; Yan, L.; Xu, Z.; Masliyah, J. Probing Adsorption of Polyacrylamide-Based Polymers on Anisotropic Basal Planes of Kaolinite Using Quartz Crystal Microbalance. *Langmuir* **2013**, *29*, 3989–3998. [CrossRef]
28. Ng, J.; Osborn, I.; Harbottle, D.; Liu, Q.; Masliyah, J.H.; Xu, Z. Stimuli-Responsive Hybrid Polymer for Enhanced Solid–Liquid Separation of Industrial Effluents. *Environ. Sci. Technol.* **2019**, *53*, 6436–6443. [CrossRef]
29. Dutta, S.; Chakraborty, S.; Sengupta, S.; Acharya, S.; Basu, D.; Bandyopadhyay, A. Genesis of an ecofriendly $A_n + B_3$ hyper-branched polyester from Poly (ethylene glycol) and aconitic acid for application as flocculant. *J. Polym. Res.* **2024**, *31*, 39. [CrossRef]
30. Zhang, Q.; Yin, Y.Q.; Xu, P.C. Experiment on properties of coal slime and its sedimentation under the action of coagulant. *Coal Eng.* **2022**, *54*, 181–186.
31. Wang, J.B. Study on the settling performance and flocculent characteristics of coal slurry water under the action of different flocculants. *Shanxi Chem. Ind.* **2024**, *44*, 100–101+117. [CrossRef]
32. Xu, D.F.; Xu, B.B.; Chang, J.J.; Zhen, J.Q.; Ma, X.M.; Zhang, C.; Wang, J. Research on Adaptive Flocculants for Flocculation and Sedimentation of Difficult-to-Settle Coal Slurry. *Coal Prep. Technol.* **2025**, *53*, 25–31. [CrossRef]
33. Wang, J.B. Influence of flocculant type variation on settling and dewatering performance of coal slurry water. *China Coal Vis.* **2023**, *1*, 154–156.

34. Lu, Y.J.; Ma, X.M.; Fan, Y.P.; Dong, X.S.; Hao, X.B.; Zhang, C. Synthesis of cationic flocculant CS-g-ADM and experimental study on coal slurry water sedimentation. *Coal Sci. Technol.* **2025**, *53*, 503–513.
35. Yang, J.N.; Zhang, Z.J. Effect of a new flocculant TG on sedimentation performance of coal slime water. *Clean Coal Technol.* **2024**, *30*, 615–621. [CrossRef]
36. Zhang, L.F.; Pang, Z.R. Application research of new coal slurry water purifying agent BK819A in a coal preparation plant in Inner Mongolia. *Coal Process. Compr. Util.* **2023**, *11*, 16–19. [CrossRef]
37. Zhang, P.P.; Zhu, X.B.; Li, W.; Fang, C.J. Study on synthesis and properties of polysilicate aluminum ferric sulfate flocculant. *Clean. World* **2023**, *39*, 63–67+71.
38. Liu, C.; Ding, X.G. Study of the coal slime water sedimentation effect obtained with the use of compound agent. *Coal Prep. Technol.* **2021**, *5*, 50–53. [CrossRef]
39. Chang, J.; Xue, J.; Liang, S.; Zhao, W.; Li, Z. Flocculation Performance and Interfacial Adsorption Mechanism of Aluminum Hydroxide–Polyacrylamide in Coal Slime Water Treatment. *Polymers* **2026**, *18*, 458. [CrossRef] [PubMed]
40. Zou, W.J. Selective Flocculation-Flotation Separation of Coking Coal's Middlings. Ph.D. Thesis, China University of Mining and Technology, Xuzhou, China, 2014.
41. Yan, L. Study of Anisotropic Surface Property of Phyllosilicates by Atomic Force Microscopy. Ph.D. Thesis, University of Alberta, Edmonton, AB, Canada, 2013.
42. Richter, R.P.; Brisson, A. QCM-D on Mica for Parallel QCM-DAFM Studies. *Langmuir* **2004**, *20*, 4609–4613. [CrossRef]
43. Ma, X.M. Study on Adsorption Behavior of Solid-Liquid Separation Chemicals at Coal Tailings Interface. Ph.D. Thesis, Taiyuan University of Technology, Taiyuan, China, 2019.
44. Li, X.; Wang, Z.; Zhang, Y.; Zhang, W.; Zhang, H.; Liu, P.; Lei, T. Hydrogen-rich gas formation from catalytic pyrolysis of biomass tar by aluminum dross coupled HZSM-5 co-loaded Ni-Fe bimetallic catalysts: Influence of co-carrier characteristics. *J. Environ. Manag.* **2025**, *389*, 126016. [CrossRef]
45. Munk, P.; Aminabhavi, T.M.; Williams, P.; Hoffman, D.E.; Chmelir, M. Some Solution Properties of Polyacrylamide. *Macromolecules* **1980**, *13*, 871–876. [CrossRef]
46. Voinova, M.V.; Rodahl, M.; Jonson, M.; Kasemo, B. Viscoelastic Acoustic Response of Layered Polymer Films at Fluid-Solid Interfaces: Continuum Mechanics Approach. *Phys. Scr.* **1999**, *59*, 391. [CrossRef]
47. Palmqvist, L.; Holmberg, K. Dispersant Adsorption and Viscoelasticity of Alumina Suspensions Measured by Quartz Crystal Microbalance with Dissipation Monitoring and in Situ Dynamic Rheology. *Langmuir* **2008**, *24*, 9989–9996. [CrossRef]
48. Dunér, G.; Thormann, E.; Dėdinaitė, A. Quartz Crystal Microbalance with Dissipation (QCM-D) studies of the viscoelastic response from a continuously growing grafted polyelectrolyte layer. *J. Colloid Interface Sci.* **2013**, *408*, 229–234. [CrossRef] [PubMed]
49. Yang, W.Y.; Qian, J.W.; Shen, Z.Q. A novel flocculant of $Al(OH)_3$–polyacrylamide ionic hybrid. *J. Colloid Interface Sci.* **2004**, *273*, 400–405. [CrossRef] [PubMed]
50. Yang, W.Y. Preparation, Dilute Solution Behavior and Flocculation Performance of Aluminum Hydroxide-Polyacrylamide Hybrid Materials. Ph.D. Thesis, Zhejiang University, Hangzhou, China, 2005.
51. Xue, J. Study on Coagulation Performance and Adsorption Mechanism of Novel Efficient Coagulant Al-PAM in Coal Slime Water. Master's Thesis, Xi'an University of Science and Technology, Xi'an, China, 2025.
52. Bartosiewicz, H.; Curcio, P. Coal Handling and Preparation Plant (CHPP) Corrosion Control and Management. Available online: https://acarp.com.au/abstracts.aspx?repId=C12055 (accessed on 16 January 2026).
53. Litvinenko, V. *XVIII International Coal Preparation Congress*; Springer: Berlin/Heidelberg, Germany, 2016.
54. Yao, C.; Song, Q.; Meng, L.; Zhong, H.; Cao, W.; Li, H.; Sun, C.Q.; Pang, S.; Zhang, L. Interfacial polarization and lattice hydrogenation enable accelerated aluminum combustion with hydrogen-rich fluoropolymers. *Chem. Eng. J.* **2025**, *521*, 167068. [CrossRef]

Disclaimer/Publisher's Note: The statements, opinions and data contained in all publications are solely those of the individual author(s) and contributor(s) and not of MDPI and/or the editor(s). MDPI and/or the editor(s) disclaim responsibility for any injury to people or property resulting from any ideas, methods, instructions or products referred to in the content.